GEOPHYSICS, VOL. 86, NO. 3 (MAY-JUNE 2021); P. 1–13, 15 FIGS., 1 TABLE.
10.1190/GEO2020-0181.1

Case History

Seismic imaging using an e-vib — A case study analyzing the signal properties of a seismic vibrator driven by electric linear synchronous motors

Bojan Brodic[1], Paul Ras[2], Richard de Kunder[3], Guy Drijkoningen[4], and Alireza Malehmir[1]

ABSTRACT

Seismic imaging characteristics of a prototype electrically driven, linear synchronous motor-based, vertical-force seismic vibrator ("e-vib") were evaluated at a site in the Netherlands. The system weighs 1.65 t and excites seismic signals with a peak force of 6.7 kN. Data were recorded along two collocated geophone-based nodal and landstreamer microelectromechanical system - MEMS-based sensor 2D seismic profiles. To obtain a broad bandwidth data set, the e-vib operated with a 1–200 Hz linear sweep. Shot gathers of the merged nodal-landstreamer data set indicated good-quality seismic data of a broadband nature. The processed merged data set demonstrates high-resolution reflections of the stratigraphic members from approximately 200 m to 2 km, with visible reflections as deep as 2.5–2.9 km. As a reference, we also processed a legacy 3D microspread data set acquired at the same site with a magnitude stronger (14.1 t, 67.5 kN) hydraulic vibrator. Comparison of our nodal-landstreamer seismic section versus 2D slices extracted from the processed microspread seismic volume suggested similar signal penetration depth and the same key marker horizons seen in both. Analysis of the reaction mass and base-plate accelerometer signals recorded with the e-vib source operating on grass and on asphalt surfaces indicates that the e-vib has low total harmonic distortion. The results obtained indicate that, although relatively small, the e-vib is capable of generating high-quality broadband seismic data.

INTRODUCTION

Vibroseis seismic sources have become the most dominantly used sources for land seismic acquisition (Bagaini, 2008; Sallas, 2010; Wei et al., 2010; Meunier, 2011; Dean et al., 2016). Generally, seismic vibrators — vibroseis seismic sources exert sinusoidal vibrations with constantly varying frequency ("sweep") into the ground over a wide and controllable bandwidth at repeatable rates. The signal excitation is achieved by transferring the force generated by the actuator between a reaction mass (RM) and a ground-coupled baseplate (Newman, 1994; Meunier, 2011). The baseplate coupling is additionally supported by a static hold-down force induced by the mass of the carrier vehicle, insulated by air bags. This enables the resulting applied force to exceed the combined weight of the RM and the baseplate. In a hydraulic vibrator, the actuator is a diesel engine-driven hydraulic system. A hydraulic pump provides hydraulic fluid flow to a servovalve controlling the oscillations of the RM inside a piston acting onto a baseplate (Sallas, 2010; Wei et al., 2010). The hydraulics inherently introduce limitations on the excitation of the energy and the signal quality, in particular at low frequencies (Bagaini, 2008; Sallas, 2010; Meunier, 2011; Rowse and Tinkle, 2016).

Manuscript received by the Editor 23 March 2020; revised manuscript received 13 January 2021; published ahead of production 10 February 2021.

[1] Uppsala University, Department of Earth Sciences, Uppsala 75236, Sweden. E-mail: bojan.brodic@gmail.com (corresponding author); alireza.malehmir@geo.uu.se.

[2] Geophysical Consultant, 2333 Leiden, Netherlands. E-mail: paul.ras94@gmail.com.

[3] Seismic Mechatronics, 5507 Veldhoven, Netherlands. E-mail: r.de.kunder@seismic-mechatronics.com.

[4] Seismic Mechatronics, 5507 Veldhoven, Netherlands and Delft University of Technology, Geotechnology Department, Delft 2628 CN, The Netherlands. E-mail: g.g.drijkoningen@tudelft.nl.

Sallas (2010) identifies three main limiting factors of the hydraulic servovalve system: (1) the maximum displacement range of RM within a piston — mass stroke, (2) the large hydraulic fluid flow necessary to move the mass at low frequencies — pump flow, and (3) the maximum displacement range of the servovalve — valve stroke. On the high-frequency end, high differential pressures in the actuator must be adjusted by the vibrator design to honor the fluid flow limits of servovalves and to prevent hydraulic circuit damage (Meunier, 2011). Although improvements in vibrator electronic controllers and custom-designed sweeps honoring the vibrator limitations (Bagaini, 2008; Dean et al., 2016), along with mechanical design improvements (high- and low-pressure fluid accumulators), reduce the aforementioned limitations (Wei et al., 2010), the mass stroke and its accurate control by appropriate hydraulic fluid flow remain the key limiting factors at low frequencies (Sallas, 2010; Wei et al., 2010; Meunier, 2011). In addition, the air bags act as a low-pass filter and the intrinsic nonlinearity of mechanics and hydraulics behind hydraulic vibrators and baseplate-ground coupling results in harmonic distortion causing detrimental effects such as harmonic noise, loss of energy, and ghost events in the data. With the recent increased interest in low frequencies and broadband seismic data acquisition (Denis et al., 2013; ten Kroode et al., 2013; Brittan and Jones, 2019; Cordery, 2020), even with the improvements made (Ras et al., 1999; Bagaini, 2008; Wei et al., 2010; Meunier, 2011; Wei and Phillips, 2013; Bagaini et al., 2014; Dean et al., 2016), maintaining broadband signal excitation over a wide bandwidth at a constant drive level and with minimal harmonic distortion remains challenging for hydraulic vibrators.

In response to these challenges, Drijkoningen et al. (2006) and Noorlandt et al. (2015) propose the use of linear synchronous motor (LSM)-driven vibrators as an alternative vibroseis seismic source. In this study, the performance and seismic imaging potential of a prototype 1.65 t (6.7 kN) LSM-driven vibrator are evaluated using a merged data set acquired combining a microelectromechanical system (MEMS)-based seismic landstreamer (Brodic et al., 2015; Malehmir et al., 2015a; Dehghannejad et al., 2017; Kammann et al., 2019) and a spread of 4.5 Hz geophone-based wireless seismic nodes. We analyze the signal bandwidth, penetration depth, and vertical resolution of the merged nodal-landstreamer data set. Additionally, we evaluate the newly acquired data against a legacy 3D microspread data set acquired at the same site using a 14.1 t (67.6 kN) hydraulic vibrator (Vermeer, 2012) for reference purposes.

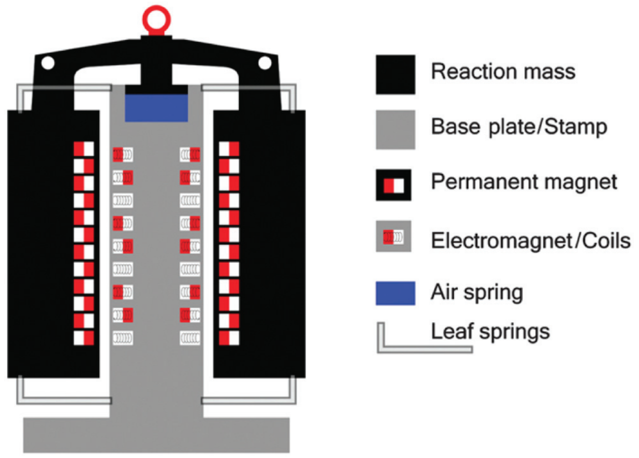

Figure 1. A 2D simplified sketch showing different components of the LSM-driven seismic vibrator (modified after Noorlandt et al., 2015). The reaction mass is separated from the base plate via leaf springs at the bottom and an air spring at the top.

LSM-DRIVEN SEISMIC VIBRATOR

As schematically depicted in Figure 1, an LSM is an electrically driven motor consisting of a magnet track and a coil track that allow the generation of large controllable forces with a reduced amount of signal distortion (Noorlandt et al., 2015). The physical idea of a hydraulically controlled RM-baseplate contact is now replaced by the interaction of a U-shaped permanent magnet track and a baseplate-connected coil track sliding in between. The current distribution over different coils controls the position of the permanent magnet RM. The intercoil and intermagnet distances were designed to enable induction of equal force for all positions. The present prototype configuration of the LSM-based seismic vibrator (six LSMs, 1027 kg RM, 230 kg baseplate, maximum driving force 6.7 kN, active stroke amplitude ±42 mm in the vertical direction, and P-wave signal excitation) enables a flat amplitude response over a sweep bandwidth of 2–200 Hz. Noorlandt et al. (2015) explain in detail that, with the current stroke, which is the determining factor for the lowest frequency, full force can be achieved at 2 Hz. Aside from the inevitable harmonics caused by baseplate-ground coupling (mostly even harmonics), the absence of hydraulics reduces the strength of the vibrator internal harmonics (mostly odd harmonics). These odd harmonics can often be prominent in hydraulic vibrators (Bagaini et al., 2014). As discussed in detail by Noorlandt et al. (2015), other harmonics and system resonances, in particular associated with the air spring, have successfully been modeled and a suppression mechanism has been developed. Differing from hydraulic vibrators, the LSM-based prototype discussed by Noorlandt et al. (2015) and tested in our study is fully electrically driven requiring 14 kW power to operate and is often called e-vib. We have accepted this term and will use it henceforth interchangeably with the LSM-driven seismic vibrator. The combined weight of the RM, the base plate (BP), and the protecting cover is approximately 1.65 t and the design enables easy attachment to locally available vehicles such as skid-steer loaders and telehandlers, among others (Storm 7, seismic-mechatronics.com/seismic-sources/storm/).

STUDY AREA AND A PRIORI INFORMATION

The test site is located near the town of Emmeloord, Noordoostpolder, Flevoland province in central Netherlands. Noordoostpolder is one of the large polders, tracts of lowland reclaimed from the sea by embankments, in the former Zuiderzee region (an inlet of the North Sea). From a geologic perspective, the near surface is represented by Holocene peat sediments formed in a shallow lacustrine environment and quaternary sands and clays deposited in a littoral marine environment. Further in depth, Neogene and Paleogene deepwater successions, subdivided by regional breaks in sedimentation into the Upper, Middle, and Lower North Sea Groups, are found. The Upper North Sea Group is mainly composed of sandstones, pebbly and calcareous sandstones, sandy shales, and claystones. The Middle and Lower North Sea Groups comprise an alteration of claystones, sandstones, and marls overlaying the chalk layer that marks the transition into the Upper Cretaceous Chalk Group and Lower Cretaceous Rijnland Group. The Chalk Group consists of chalk and flint-rich chalk successions, whereas the Rijnland Group is represented by marls and glauconite-rich sandstones. At the site, the stratigraphic profile is not fully developed and the Cretaceous sediments are sitting atop Carboniferous rocks of the Limburg Group deposited during the Silesian period. Here, one can distinguish coal and/or organic-rich or -poor successions of shales and sandstones of the Step Graben, Hospital Ground, Maurits, Ruurlo, and Epen Formations (Rijks Geologische Dienst, 1993; Wong et al., 2007; Kombrink et al., 2012). Figure 2 shows the location of the site and the seismic profiles analyzed in this study, along with a simplified stratigraphic column with the approximate depths and thicknesses of the lithologic units. The stratigraphic column was compiled using the information available online from the Geological Survey of the Netherlands (Rijks Geologische Dienst) and the results shown in Rijks Geologische Dienst (1993), Kombrink et al. (2012), and Munsterman et al. (2012).

Additionally indicated by the black asterisk in Figure 2, and described in detail in Figure 3, is a 2.6 km deep exploration well (EMO-01) located approximately 10 km away from the study site that will be used to constrain our results. The logging information available from the Geological Survey of the Netherlands includes sonic, density, gamma ray, neutron logs, and approximate P-wave interval velocities and corresponding two-way traveltimes (TWT) until the depth of approximately 2.6 km (Figure 3).

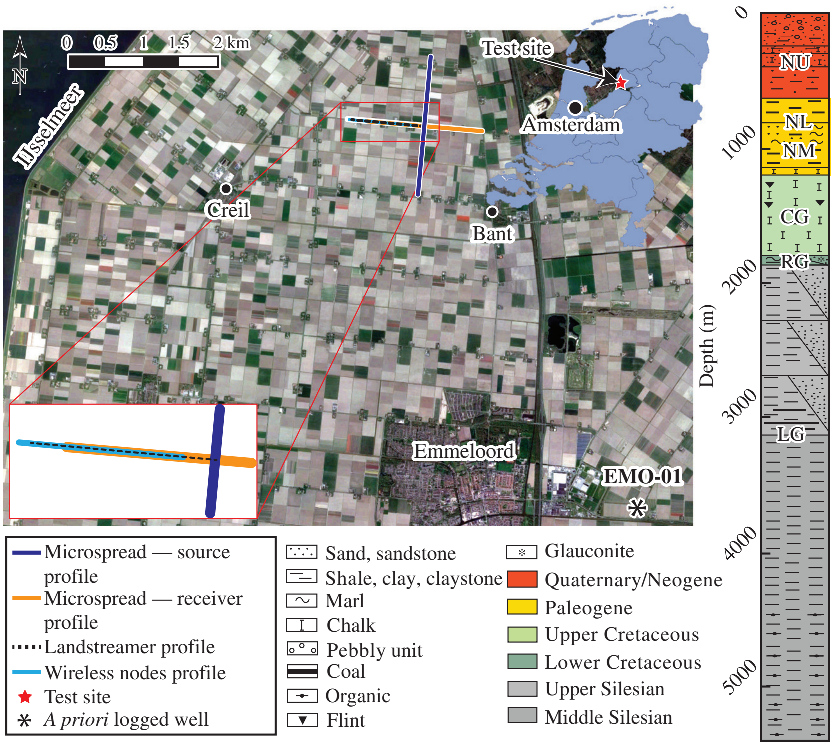

Figure 2. An aerial photo showing the location of the study site and the different seismic data sets analyzed in this study, together with a stratigraphic column showing various geologic units and formations in the study area and the a priori available EMO-01 exploration well (the black asterisk). NU, Upper North Sea Group; NL and NM, Lower and Middle North Sea Group; CG, Chalk Group; RG, Rijnland Group; LG, Limburg Group. An enlarged view of the overlapping portion of different seismic data sets, marked by the red rectangle, is also shown as an inset figure. The 3D microspread source line is shown in dark blue, the receiver line in orange, the landstreamer in dashed black, and the nodal spread in light blue.

SEISMIC DATA SETS

The site history makes it a land analogous to the North Sea marine environments and, together with available wells, motivated earlier seismic surveys by Shell and the Delft University of Technology and also us to use it for the seismic experiment. Our analysis is based on two seismic data sets with the primary focus on a newly acquired (December 2018) nodal-landstreamer seismic data set. The second data set analyzed is a legacy 3D microspread (Vermeer, 2012) that will be used as a reference for evaluating the reflection seismic potential and signal quality of the nodal-landstreamer data set.

Newly acquired nodal-landstreamer seismic data set

To evaluate the seismic imaging properties of the e-vib, a seismic survey was conducted using a dual-element seismic spread. The first element consisted of a 2D seismic profile covered with 251 wireless seismic recorders — nodes with 4 m intervals. All nodes were connected to 4.5 Hz, either 1C or 3C geophones (every second station). The second portion of the spread involved deploying a 3C MEMS-based seismic landstreamer (Brodic et al., 2015, 2018; Malehmir et al., 2015b; Malehmir et al., 2017) at 1 m lateral offset from the wireless nodes. To enable recording data with a maximum offset of approximately 1.2 km, the first landstreamer sensor was positioned 200 m ahead of the first wireless node. The total length

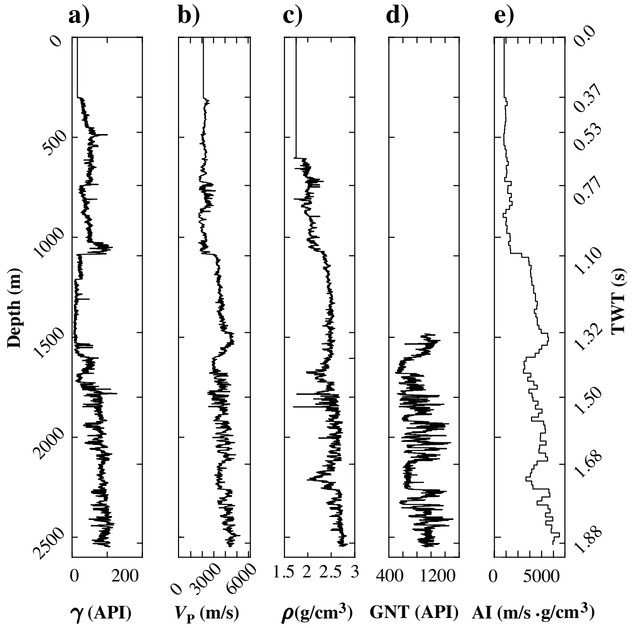

Figure 3. A priori available well-logging information from the EMO-01 well showing (a) natural gamma, (b) sonic, (c) density, and (d) neutron log (GNT). (e) Calculated acoustic impedance log (AI) and the corresponding TWT down to the depth of 2.6 km.

of the landstreamer was 240 m with 100 MEMS-based sensors mounted on five different segments. Eighty sensors (mounted on four segments) are 2 m apart, whereas the last twenty (one segment) has sensors with 4 m intervals. The prototype LSM-driven seismic vibrator was mounted on a locally available telehandler and used as the source. The source points were 8 m apart along the entire combined nodal-landstreamer spread with the first shotpoint collocated with the first landstreamer sensor. After acquiring data along the first landstreamer position, the landstreamer was towed forward for 160 m and the shooting continued with 8 m source spacing. The procedure was repeated seven times to acquire in total a 1.2 km long seismic profile, while always keeping an overlap of the 80 m long streamer segment (20 sensors at 4 m) between subsequent streamer positions. A 20 s long linear sweep ranging from 1 to 200 Hz with a peak force of 6.7 kN with an additional 5 s recording time was used. Every vibrating point consisted of two sweeps that were vertically stacked to improve the signal-to-noise ratio (S/N). The landstreamer data were recorded using a Sercel Lite acquisition system at a 1 ms sampling rate without applying any recording equipment filters (neither low- nor high-cut). All wireless nodes were operating in an autonomous mode (1 ms sample rate), and microsecond-accuracy GPS time stamps of every sweep initiation were used as a common base to merge the two data sets. Figure 4a shows a sketch of the seismic spread and acquisition methodology used, along with a field photo (Figure 4b) showing the source tested in this study mounted on the carrier vehicle and a photo showing the source with the cover removed (Figure 4c).

Legacy 3D microspread

Seismic microspreads or noise spreads have traditionally been used to determine the optimal choice of shots and receivers, minimally required fold, and detailed investigation of the seismic wavefield enabling optimization of the survey design parameters. With this in mind, in 1992, a 3D seismic microspread (cross-spread with small source-receiver intervals) was acquired by Shell Research at the same site used for our test (Chapter 7.2 in Vermeer, 2012). The spread consisted of 960 source and receiver locations at 2 m spacing, acquired in two passes along the source line using 480 active channels. In the first pass along the source line, the left half of the receiver spread was acquired followed by the right half. The nearest source point was 1 m offset in the crossline direction from the receiver line, and the maximum inline offset was 959 m. A single hydraulic vibrator weighing approximately 14.1 t with a peak force of 67.6 kN was used as the seismic source with a single 27 s linear sweep ranging from 8 to 60 Hz (Vermeer, 2012). Data were recorded using a sampling rate of 4 ms. Figure 2 details locations and overlapping portions of the two data sets analyzed in our study.

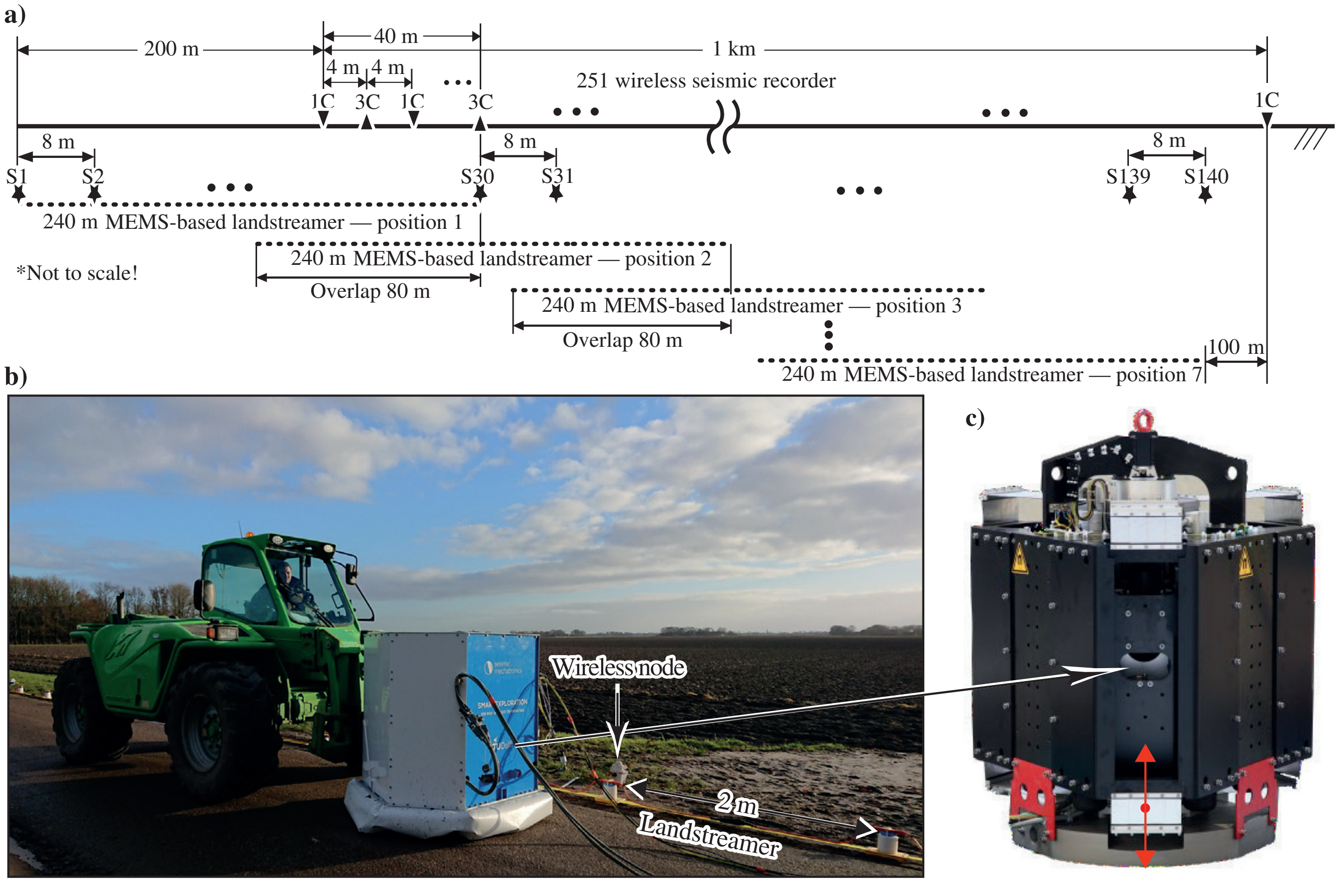

Figure 4. (a) Sketch showing the seismic spread used for the December 2018 data acquisition with "S" marking the vibrating points and "1C" and "3C" standing for the single- and three-component wireless nodes, respectively. (b) The 1.65 t LSM-driven vibrator at one source location next to the seismic landstreamer and its corresponding carrier vehicle. (c) An enlarged view of the source internal design and energy polarization direction illustrated by the red arrows. Photo by EAGE BV, December 2018.

An example microspread source gather with its frequency-wavenumber (*f-k*) domain plot and the corresponding amplitude spectrum are shown in Figure 5.

Signal analysis of the e-vib seismic source via the nodal-landstreamer data set

The overall S/N of the newly acquired data set was relatively high (Figure 6), with some records showing a strong presence of wind and ground roll noise. The former is particularly notable as moderately dipping off-plane noise. Because the legacy 3D microspread was acquired using a vertical seismic vibrator with vertical geophones only, and because the e-vib tested is also a vertical vibrator, we restrict our analysis to only the vertical component of the 3C receivers. The vertical components of all receivers are analyzed after vertical stacking of the repeated sweeps. For all of the comparisons made in the study, the landstreamer MEMS acceleration data are integrated followed by a 4 Hz, cosine-tapered, low-cut filter to maintain the velocity domain and phase consistency of the nodal-landstreamer and the microspread data. Selection of the low-cut filter frequency and taper was based on obtaining a similar amplitude response as for the 4.5 Hz geophones used on the nodal portion of our seismic spread. Figure 6a shows a merged nodal-landstreamer shot gather, and Figure 6b and 6c, respectively, shows its frequency-wavenumber (*f-k*) domain plot and the amplitude spectrum after pilot crosscorrelation and vertical stacking of the repeated sweeps. To analyze the effect of the MEMS acceleration-to-velocity transform, Figure 7a and 7b shows enlarged views marked by the red rectangle in Figure 6a of the merged nodal-landstreamer data before and after the transform, respectively. Shown in Figure 7c are the amplitude spectra of merged velocity domain data, geophone-based nodal only, and MEMS before and MEMS data after integration, as indicated by different colors. The spectra are plotted using a logarithmic scale to illustrate the effect of the transform applied on frequencies less than 10 Hz.

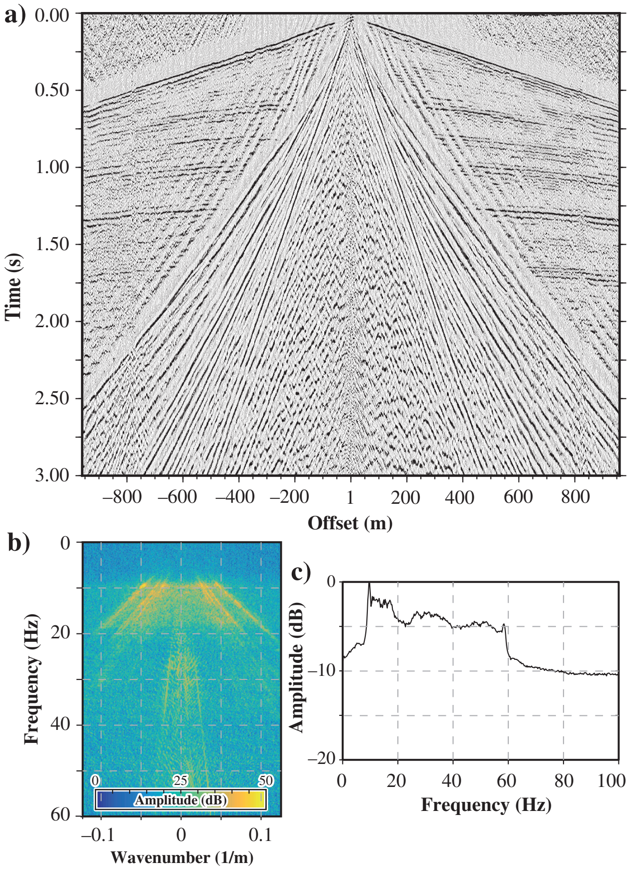

Figure 5. (a) An example shot gather extracted from the 3D legacy microspread data set with (b) its frequency-wavenumber (*f-k*) domain pair and (c) the corresponding amplitude spectrum. Note that the source is located at a 1 m lateral offset from the receiver line. For display purposes, a 250 ms long automatic gain control (AGC) window is applied.

Figure 6 illustrates the relatively strong presence of wind noise and ground roll masking the deeper events. Clear reflections are visible in the optimal window portion of the shot gather. Longer offsets of the microspread data (Figure 5) extend the optimal window, enabling clearer recognition of events down to approximately 1.7 s. Similar to e-vib data (Figure 6), strong ground roll and source-generated noise mask the recognition of any reflections within the noise cone of the microspread data (Figure 5). The *f-k* plot in Figure 6b shows a clear differentiation of different surface-wave modes and a certain amount of spatial aliasing caused by the 4 m spacing of the nodal portion of the seismic spread. We can also see that the ground roll contains very low frequencies starting at 1–2 Hz confirming the low-frequency output of the e-vib and demonstrating the potential for surface-wave inversion and/or full-waveform inversion. Comparing Figure 7a and 7b, the phases of the merged nodal-landstreamer data set appear consistent after integrating the MEMS data. Minor differences between wavelet shapes can be attributed to noncollocated receivers.

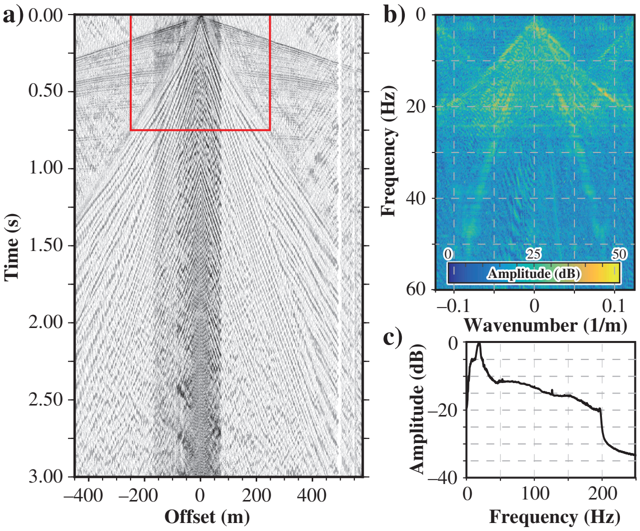

Figure 6. (a) Typical quality combined nodal-landstreamer shot gather after transferring the MEMS acceleration into the velocity domain with (b) an *f-k* plot and (c) the accompanying amplitude spectrum of the same gather. The red rectangle in (a) marks a portion of the gather that will be used to further analyze the effect of transferring the MEMS accelerometers data into the velocity domain. For display purposes, a 250 ms AGC was applied and (a and b) were plotted using the same parameters and offset scale as in Figure 5.

SEISMIC IMAGING, SIGNAL PENETRATION DEPTH, QUALITY, AND BANDWIDTH

To evaluate the signal bandwidth and maximum penetration depth of the e-vib, we processed the 3D legacy microspread and our merged data set. Both data sets were processed in a standard manner aimed at noise attenuation and bandwidth preservation with the processing steps shown in Table 1. For stacking purposes, the same normal moveout (NMO) velocity model was used for both data sets. The interval velocities of the EMO-01 borehole, combined with the NMO velocities of prominent events and analysis of constant velocity stacks (CVS), were used to build the stacking velocity model. For the merged data set, due to the 4 m spacing of the wireless nodes, a 2 m common midpoint bin size and a straight-line geometry were selected. An orthogonal geometry with bin sizes of 2 m (to keep the same size with the former as a reference purpose) in the inline and crossline directions were used for producing the 3D microspread NMO-corrected seismic cube. Except for the median filter to attenuate strong S-wave arrivals in the microspread data set, MEMS integration of the merged data set and individually adopted deconvolution, and spectral equalization parameters, the prestack processing steps were kept consistent.

Figure 8 shows two example 2D inline slices extracted from the unmigrated NMO-corrected stacked seismic volume of the 3D microspread. An inline with the source at an offset and one with the source near the receiver line are shown to demonstrate the effect of source-generated noise on the quality of the processed seismic volume. Note the incompletely removed S-wave after application of the median filter starting at approximately 2.25 s in Figure 8a in the center of the section. Figure 8b shows that the *f-k* filter was only partly able to suppress the ground roll, likely due to the emphasis on the lower frequencies in the sweep (an 8–60 Hz sweep was used). Considering that the nominal fold is 2, both 2D slices shown in Figure 8 show a relatively good quality seismic data with strong reflections down to 1.6 s and visible ones until approximately 2.25 s. The depth-to-time conversion was obtained using a checkshot-corrected sonic log data from the EMO-01 well (Figure 3b). Also shown in Figure 8, as a red trace overlaid on top of the two 2D inline slices, is a zero-offset synthetic seismogram. The synthetic seismogram was obtained from the EMO-01 well-log data, blocked using 20 m intervals and generated with an 80 Hz Ricker wavelet (Levendal et al., 2019). The center frequency of the Ricker wavelet was selected to conform with the average frequency of the e-vib merged data set.

Given that the EMO-01 borehole is approximately 10 km away from the test site, the synthetic seismogram was tied to the merged stacked section as shown overlaid on top of the processed merged seismic section in Figure 9. The time shifts, hence, the tie between the synthetic and the field seismic trace, were accomplished via a sliding window crosscorrelation routine (Margrave and Lamoureux, 2019). The red square shown in Figure 9 marks the overlapping portions of the microspread and our merged data sets, and it marks the portion of the merged seismic section used for the bandwidth analysis shown in Figure 10. In addition to different filter panels, Figure 10 (the furthest to the right) also shows the overlapping portions of our merged data set and inline 1050 shown in Figure 8a. Apart from the higher resolution due to a broadband sweep and increased fold, the same key reflections matching the microspread data can be seen on the e-vib merged data set and the penetration depth appears the same. Key markers in Figures 8 and 9 and the panels shown in Figure 10 are in accordance with the synthetic zero-offset seismogram. Compared to the e-vib stacking result (Figure 9), the microspread results show that S-wave, ground roll, and source-generated noise were only partly suppressed on the microspread data using standard processing algorithms. The near-offset source-generated noise on the microspread data was very problematic and could not be entirely suppressed. Figure 8b demonstrates the signal deterioration due to the source vicinity with only a portion of the strong reflections notable within the noise cone. Because this noise type was not notable on the e-vib merged data set, it is likely an effect of a much larger size vibrator (14.1 t) and more time spent in the low frequency (ground roll-generating) part of the sweep. Focusing on the frequency panels of the e-vib stacked section shown in Figure 10, we can see that strong reflection energy down to around 1.65 s (2 km) can be seen from approximately 10 to 75 Hz. In the frequency bands from 10 to 100 Hz, strong reflection energy is present down to roughly 1.25 s (1.3 km). In the shallow portion

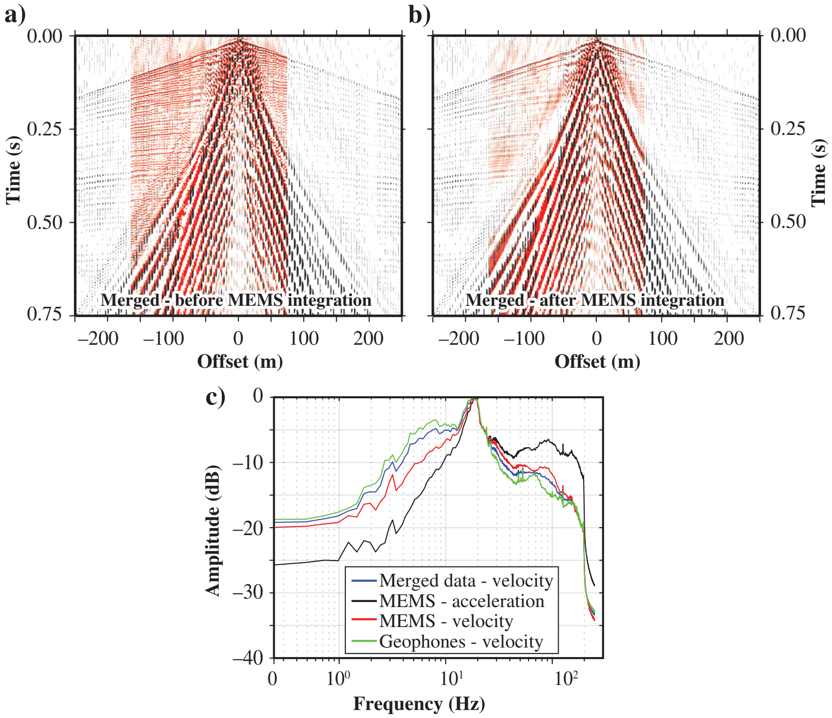

Figure 7. Enlarged views marked by the red rectangle in Figure 6a illustrating the phase consistency and discrepancy of the MEMS accelerometers (a) before and (b) after integration, respectively. The red traces correspond to the MEMS landstreamer, whereas the black ones are the geophone-based nodal receivers. Different colors in (c) correspond to the amplitude spectra of individual and merged nodal-landstreamer portions of the seismic spread as annotated on the graph with the MEMS spectra shown before and after integration plotted using a logarithmic scale.

(approximately 0.25 s) of the merged stacked section, the reflection energy is present up to a maximum frequency band of 150–160 Hz. Weak coherency events can be seen in the 160–170 Hz band, whereas bands greater than 170 Hz show no coherent events. Although it is only 6.7 kN, the e-vib seismic source is capable of producing good-quality seismic data from 200 to 2 km and visible reflections down to 2.5–2.9 km in depth.

Analysis of the vertical resolution and harmonic distortion

Focusing on the results shown in Figures 8 and 9, although a significant difference exists between the acquisition parameters and peak forces of the two seismic sources (hydraulic vibrator versus e-vib) used to acquire the data, similar signal penetration depth with prominent key reflections is notable on both. This is also partly supported by shot gathers of both data sets where key reflections can be noted on both (Figures 5 and 6). Considering the low-fold nature (fold of 2) of the microspread data set, the comparison is made as a reference point and in a purely qualitative approach. To further evaluate the signal quality of the e-vib merged data set and the reflections seen in Figures 9 and 10, Figure 11 compares the frequency content and vertical resolution of the e-vib data. Figure 11a shows curves for the interval velocity (V_{int}), average velocity (V_{ave}), and root-mean-square (rms) velocity (V_{rms}) derived from the EMO-01 borehole. We have used the filter bands extracted from the e-vib seismic section (Figure 10) to estimate the bandwidth in terms of the maximum frequency $F_{\max}$ (the maximum frequency based on a sinc wavelet), dominant frequency F_{dom} (the dominant frequency of a Ricker wavelet), and peak frequency F_{peak} (the peak frequency of a Ricker wavelet). The relationships between these frequencies are as follows: $F_{\mathrm{dom}} = 0.7F_{\max}$ and $F_{\mathrm{peak}} = 0.54F_{\max}$ (Kallweit and Wood, 1982). The resulting frequency plots are shown in Figure 11b. The maximum frequencies were selected based on visual inspection of coherency of the prominent reflections in different frequency bands shown in Figure 10. Using the dominant frequency and interval velocities, we can estimate the vertical (thin-bed) resolution, using $\lambda/4 = V_{\mathrm{int}}/(4F_{\mathrm{dom}})$ criteria, also called the tuning thickness. We observe that, with a maximum frequency of approximately 100 Hz at the Cretaceous target horizons at 1.5 s (1.8 km depth), one can achieve a vertical resolution of 10–15 m, as shown in Figure 11c.

In addition to being capable of inducing low-frequency energy at a constant drive level, an important aspect of a seismic vibrator is to generate and radiate synchronous and repeatable sweeps into the ground. To ensure a consistent fundamental wavelet and

Table 1. Processing steps applied to the different receivers and data sets.

Step	e-vib 2018 — merged	Legacy 3D microspread
1	Read raw SEGD (MEMS landstreamer + nodal data sets)	Read SEGY data
2	Crosscorrelate with pilot	—
3	Vertical stack repeated sweeps	—
4	Remove all but the vertical component	—
5	Convert MEMS acceleration into the velocity domain	—
6	Merge landstreamer and nodal data	—
7	Add geometry (CDP spacing 2 m)	Add geometry (CDP spacing 2 m)
8	Balance amplitudes (entire trace)	Balance amplitudes (entire trace)
9	Dip filter via the f-k_x domain (ground roll, wind noise)	Dip filter via the f-k_x domain (ground roll, wind noise, source-generated)
10	Elevation statics	Elevation statics
11	Refraction statics (rms = 1.8 ms)	Refraction statics (rms = 2.8 ms)
12	Spherical divergence correction	Spherical divergence correction
13	Predictive deconvolution (gap 10 ms)	Predictive deconvolution (gap 15 ms)
14	Attenuate airwave (median filter)	Attenuate airwave (median filter)
15	—	Attenuate S-wave (median filter)
16	LMO-based top mute of direct and refracted arrivals	LMO-based top mute of direct and refracted arrivals
17	Velocity analysis (CVS + borehole info)	—
18	NMO corrections (50% stretch mute)	NMO corrections (50% stretch mute, the same velocity function as for e-vib)
19	Spectral balancing (15–20–140–160 Hz)	Spectral balancing (10–20–50–60 Hz)
20	AGC (100 ms)	AGC (100 ms)
21	Stack (normal)	Stack (normal)
22	Wiener deconvolution via the f-x domain (25 traces, 100 ms)	Wiener deconvolution via the f-x domain (25 traces, 100 ms)
23	—	Dip filter via the f-k_x domain (remaining source-generated noise)
24	AGC (500 ms, for display purposes)	AGC (500 ms, for display purposes)

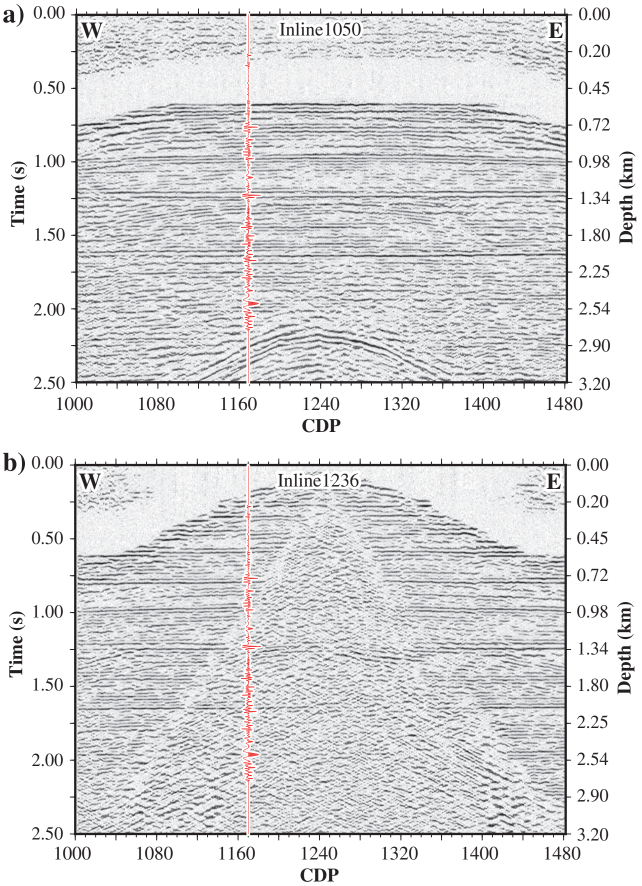

Figure 8. Two example 2D inline slices extracted from the processed NMO stack seismic volume of the 3D microspread. (a) Inline 1050 at the far offset and (b) inline 1236 at the near offset to the receiver line. The red trace overlaid on the inlines is a 1D synthetic seismogram obtained from the EMO-01 well log data. Note the effect of the source offset on the S/N. The common depth point (CDP) spacing is 2 m. For processing purposes, AGC was applied.

compensate for vibrator-ground coupling, seismic vibrators are equipped with different vibrator feedback control loops (Wei et al., 2010). The most commonly accepted method for vibrator feedback control is based on the use of a weighted-sum ground force (GF) signal for "phase locking" of the pilot signal (Sallas, 1984, 2010). Given that the e-vib tested in our study does not have a vibrator control system, we have tried to estimate whether this absence results in any prominent harmonic distortion. Here, we have focused on analyzing signals recorded using four built-in accelerometers (three on the RM and one on the BP), calculated GF and the pilot signal (Pilot), with the source point located on different ground conditions, namely, grass versus asphalt surfaces. Although to acquire our nodal-landstreamer data set, all of the source points were on asphalt, at the end of the acquisition, the e-vib was moved to the grass next to the asphalt road to obtain input data for evaluating its operation on a softer surface. The GF was estimated as the sum of the RM and BP accelerometer signals multiplied by their respective masses (Sallas, 1984; Ghose, 2002; Wei, 2009; Wei et al., 2010). Figure 12 shows the time-domain accelerometer signals, pilot signal, and computed GF for a vibrating point located on grass. Figure 13 shows the same signals as Figure 12, with the vibrating point located on asphalt. Figures 12b–12d and 13b–13d show enlarged views of RM, BP, and pilot signals, whereas Figures 12f–12h and 13f–13h show enlarged views of the pilot and GF signals corresponding to the times annotated on the lower axis. Different ground conditions are most prominently observed on the BP accelerometer signals, demonstrating an entirely different amplitude response for asphalt (Figure 12a) versus grass (Figure 13a). The computed GF signals for both surface conditions are similar up to about half of the sweep duration, after which the higher frequencies are more attenuated on the softer ground (Figure 12e versus Figure 13e). Comparing Figures 12c and 13c, a certain phase shift is notable between RM, BP, and pilot signals, whereas comparison of Figures 12g and 13g shows a 180° phase shift between the GF and the pilot. This effect is present irrespective of the ground conditions in the center time of the sweep. The phase discrepancy is negligible in the beginning and decreases toward the end of the sweep time. However, as expected, the stiffer asphalt surface distorts the BP signal more compared to the grass, introducing additional phase shift and amplitude differences (Figures 12c and 13c).

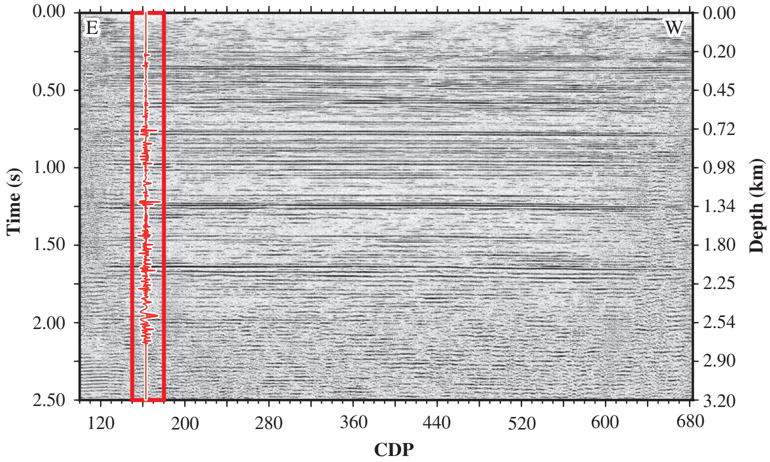

Figure 9. Processed unmigrated stacked section of the e-vib merged data with the red rectangle marking the enlarged view of the corresponding CDPs used for the signal bandwidth analysis shown in Figure 9. The red trace overlaid is the 1D synthetic seismogram obtained from the EMO-01 well log data. Note the good-quality reflections from 200 to 2 km and the visible ones down to approximately 2.9 km depth. The CDP spacing is 2 m. For processing purposes, AGC was applied.

We also evaluated the accelerometer signals in the frequency-time (FT) domain. Figure 14 shows FT spectrograms of RM, BP, and GF where we can see the relative strength of the harmonics versus the fundamental sweep and we can also get an idea of the impact of the ground conditions — grass (Figure 14, the left column) versus asphalt (Figure 14, the right column). The dynamic range of the frequency-time plots is 80 dB, and the main events are the fundamental, second, and third harmonic. We observe that on the soft and stiff ground conditions the harmonics are at least 30 dB down from the fundamental.

We additionally tried to estimate the total harmonic distortion (THD, as %), particularly at the low frequencies where hydraulic vibrators often struggle. This was done by transferring the time-domain signals into the FT domain and estimating the amplitude ratio between the fundamental and the sum of the second, third, and fourth harmonics at discrete frequencies. Figure 15 combines the FT domain plots of the computed GF signals, with the dynamic range reduced to 50 dB, for both surface conditions (grass versus asphalt) and the result of the THD estimates. For the asphalt case (Figure 15a), we observe that the second harmonic (which is generally assumed to be due to the baseplate-ground interface — see, e.g., Wei et al., 2010, Wei and Hall, 2011, or Wei and Phillips, 2013) — is at least 30 dB down from the fundamental. On grass (Figure 15b), the third harmonic (generally assumed to be due to the vibrator mechanics) is still visible; whereas on asphalt (Figure 15a), it can no longer be observed, i.e., it is more than 50 dB down from the fundamental. Figure 15c shows the THD, averaged between the two different ground surfaces, grass and asphalt, for BP and GF signals as a function of frequency. For the GF, which is representative of the vibrator itself, we find values of 8% at 7.5 Hz, 2% at 15 Hz, and <1% at frequencies of 25 Hz and higher (Figure 15c). The distortion values for the GF, which are averaged between grass and asphalt, appear significantly lower than what we normally expect for hydraulic vibrators. For example, Tellier et al. (2014) show hydraulic vibrator distortion values of 50% at 7.5 Hz and 10%–20% at 15 and 25 Hz, but they give few details about the ground conditions and, obviously, the force level used in their setup is much higher. However, without a direct comparison being available, it is difficult to quantify this difference.

DISCUSSION

With the recent trend of increased interest in low-frequency or broadband seismic data acquisition, Drijkoningen et al. (2006) and Noorlandt et al. (2015) propose the use of an LSM-driven electric seismic vibrator operating with a constant drive level and providing a flat amplitude response within the 2–200 Hz bandwidth. The details of the design and the issues that had to be resolved during the design stage are discussed in detail in Noorlandt et al. (2015), and we focus only on the seismic imaging potential of

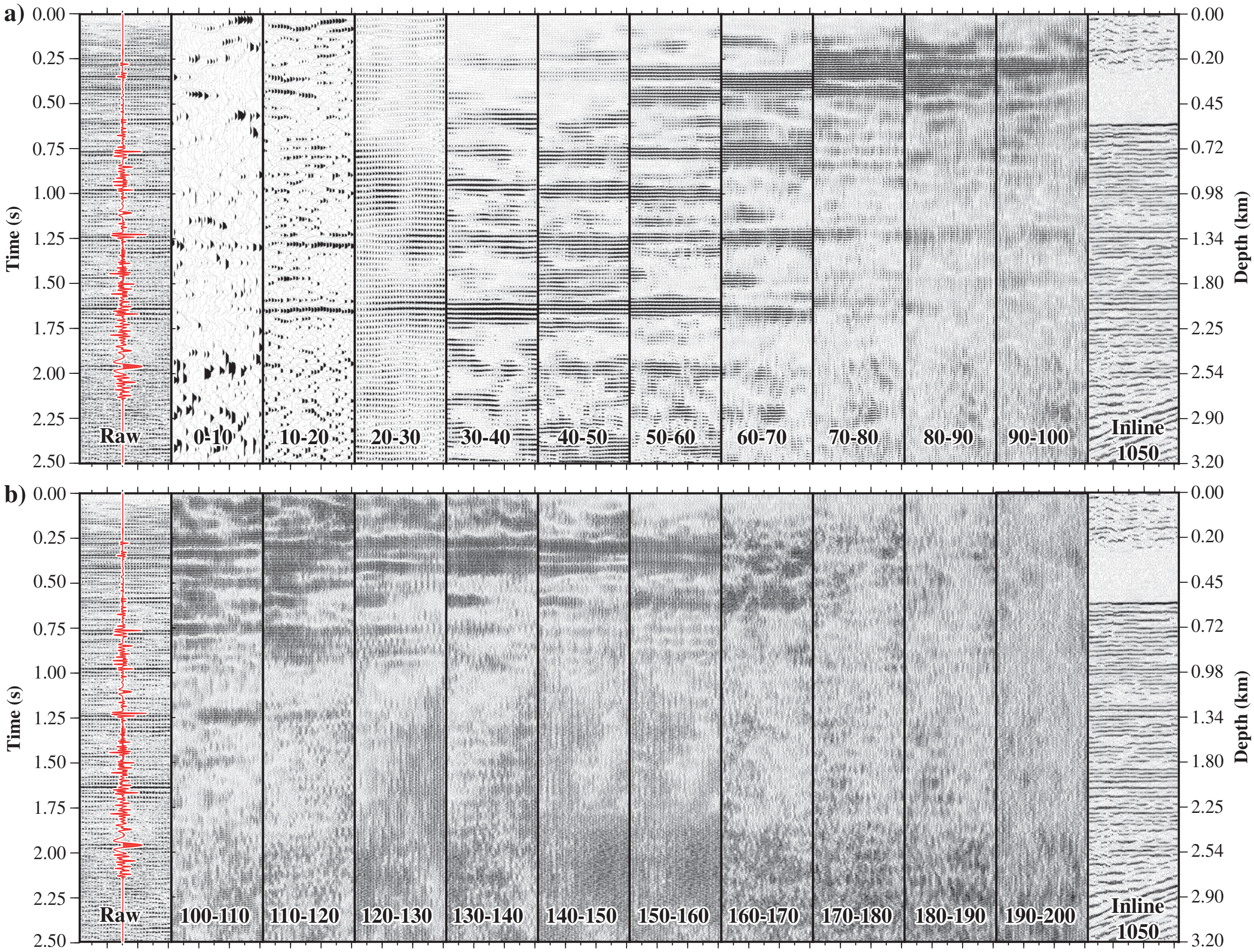

Figure 10. Frequency band analysis of a portion of the merged seismic section shown in Figure 9 by the red rectangle with (a) showing the frequencies of less than and (b) the frequencies of greater than 100 Hz. For reference purposes, the rightmost panels in (a and b) show the overlapping portion of the e-vib stacked section with a portion of the inline 1050 shown in Figure 8a. The corresponding frequency band is annotated at the bottom of every plot. The red trace overlaid is a 1D synthetic seismogram obtained from the EMO-01 well log data. For display purposes, trace normalization after stacking was applied.

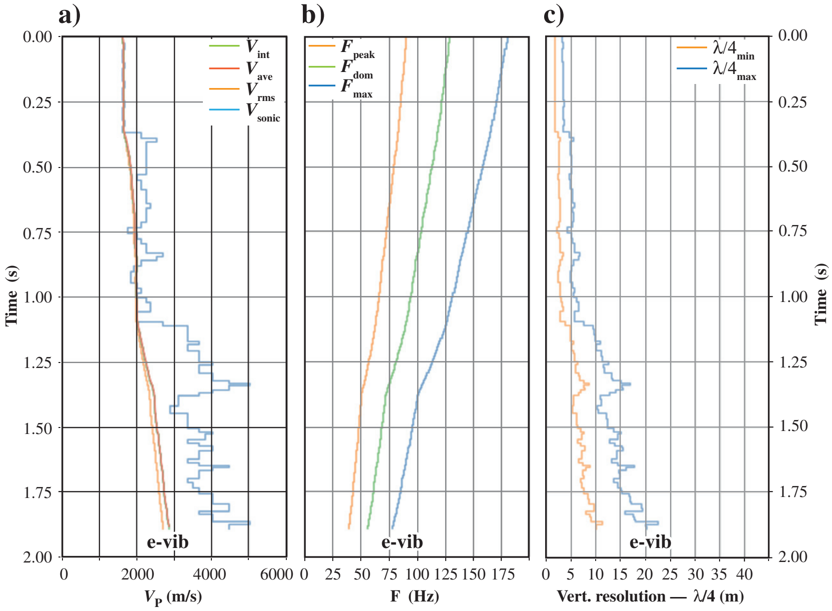

Figure 11. Frequency and resolution analysis of the data acquired using the e-vib seismic vibrator. (a) Velocity models obtained from the EMO-01 borehole, (b) maximum, peak, and dominant frequencies obtained from the e-vib stacked section frequency panel analysis (Figure 10a and 10b), and (c) calculated vertical resolution using the frequencies shown in (b) and the velocities in (a). Note that the vertical resolution at the Cretaceous target horizons at 1.5 s (1.8 km depth) is 10–15 m.

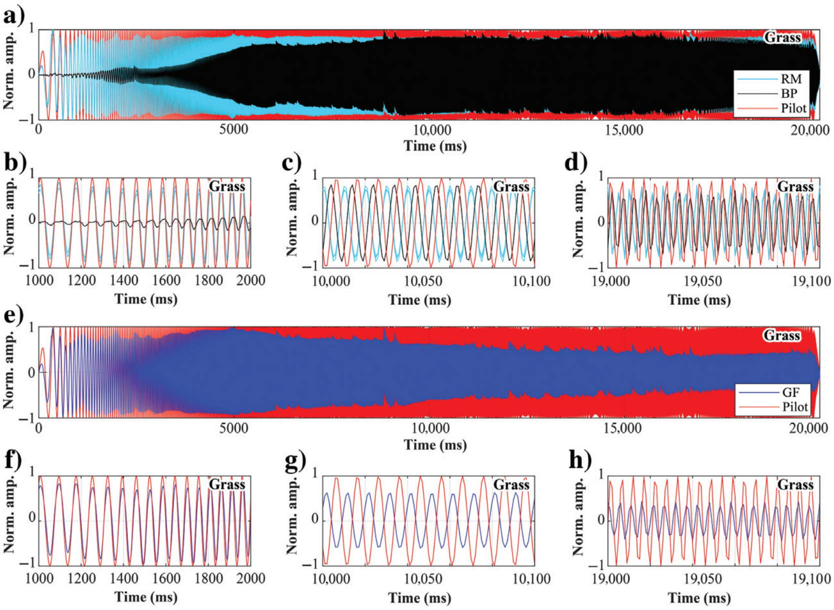

Figure 12. Evaluation of signals recorded with the reaction mass (RM) and base plate (BP) accelerometers versus pilot signal (pilot) and computed ground force (GF) signal for the vibrating point located on grass. (a) Overlay of the BP, RM, and pilot signal for the entire 20 s sweep. (b–d) Enlarged views of the signals shown in (a) at times annotated on the lower axis of every plot. (e) Comparison of the pilot (red) versus GF signal (blue) for the entire 20 s sweep. (f–h) Enlarged views of the signals at the times annotated on the lower axis of every plot. The colors represent different signals as annotated in legend in (e).

the LSM-driven seismic vibrator. In addition to the LSM-driven vibrator evaluated in this study, Teyssandier and Sallas (2019) report on a marine vibrator, also driven by linear motors. Although their paper does not discuss the design details, they report similar levels of harmonic distortion as shown in Figures 14 and 15, indicating the potential of the LSM design for both land and marine seismic data acquisition.

Analyzing the raw e-vib shot gather (after correlation and acceleration to velocity transform) depicted in Figure 6, a broad bandwidth with shallow (0.1 s) and traces of deeper reflections outside of the noise cone portion down to approximately 1.5 s can be observed. The deeper events are in accordance with the legacy microspread gather shown in Figure 5. However, their energy is inevitably far lower due to the much smaller source size. Nonetheless, despite being rather small (1.65 t, 6.7 kN), the e-vib was capable of producing good-quality seismic data, encouraging us to proceed with processing. The merged nodal-landstreamer data set was processed and evaluated in terms of its imaging potential against the 3D microspread data set as a reference.

Noise attenuation for reflection seismic processing of both data sets was troublesome, largely due to the strong ground roll and wind noise. Numerous iterations of *f-k* filtering were necessary to suppress these noise types, on the merged and on the 3D microspread data set. Compared to the merged data set in which the *f-k* filter was able to suppress most of the unwanted noise, strong source-generated noise could be only partly suppressed on the microspread data set. This effect is prominent when comparing Figures 8 and 9. In the processing results of the microspread data, a significant amount of noise can be seen in the 2D inline slices extracted from the NMO stack seismic volume, particularly when the source approaches the receiver line. Whether this effect is due to a heavier source generating more low-frequency ground roll, the low-frequency nature of the sweep used, the cross-spread geometry, or maybe that vertically stacked e-vib vibration points enhance the reflected energy within the noise cone is unclear. Compared to Figure 8, the merged e-vib seismic section shown in Figure 9 appears entirely free of the aforementioned noise types with good quality reflections notable down to 2 km and visible ones to 2.5–2.9 km depth.

Bandwidth analysis with filter panels (Figure 10) demonstrates that a small 6.7 kN e-vib is capable of generating broadband seismic signals from 10 to 180 Hz in the shallow (<200 m) and deep (>2 km) portions of the seismic section. The well tie with the seismic section confirms the seismic events and penetration depth. Analyzing the 0–10 Hz frequency band (Figure 10a), some coherent energy at approximately 1.25 s can be seen, but, judging from the *f-k* plot shown in Figure 7b, it appears that ground roll dominates the lowest frequency band. To generate the lowest frequencies as the reflection signal, more low-frequency energy, i.e., a bigger (heavier) vibrator and/or a tailored sweep (e.g., low dwell), is likely needed. On the high-frequency side, the resolution analysis in Figure 11 demonstrates the broadband output resulting in 10–15 m vertical resolution at the Cretaceous target horizons at 1.5 s TWT (1.8 km depth), indicating the importance of broadband seismic signal excitation (Denis et al., 2013; ten Kroode et al., 2013; Cordery, 2020).

Bearing in mind that the e-vib currently does not have a built-in force-feedback control, an attempt was made to evaluate if this absence could be compensated by GF deconvolution (Ghose, 2002). No significant changes were observed when comparing pilot and GF cross-correlated versus GF deconvolved data. However, given that the data were processed with AGC and high ambient noise levels, whether a different result would be obtained via true-amplitude processing remains unclear. As a part of the harmonic distortion analysis, further evaluations were made to see if harmonic distortion was visible at negative correlation times, which was not the case. The results of both of these are omitted to avoid redundancy. The two aforesaid analyses were conducted to evaluate if the occasional phase discrepancy between GF and the pilot signals (reaching almost 180° in the center of the sweep; Figures 12g and 13g) and/or other differences observed in BP and RM signals for different ground conditions (Figures 12 and 13) have a significant effect on the data quality. Considering that the peak force that the source induces in the ground is rather low (6.7 kN), this low force is likely the main reason why low distortion, no significant energy in the negative correlation times, or improvements after GF deconvolution can be observed. The same effect might explain why, although we observe certain frequency-dependent and ground-dependent phase distortion between BP and RM and therefore on the GF (Figures 12 and 13), we could not see any adverse effects in the data itself. At this stage, no explanation for this frequency-dependent phase distortion effect is found and this requires further research. All of the aforementioned analyses, and the FT domain harmonic distortion analysis shown in Figures 14 and 15, were enabled by the four e-vib built-in accelerometers. The harmonic distortion analysis indicates that the harmonic distortion was slightly less on asphalt compared to grass and that THD levels for the GF (Figure 15c), which is representative for the vibrator internally, are generally quite low and likely lower than for a hydraulic vibrator (Bagaini, 2008; Wei et al., 2010; Wei and Hall, 2011; Wei and Phillips, 2013; Bagaini et al., 2014). However, given that the e-vib has a peak force of only 6.7 kN, to support

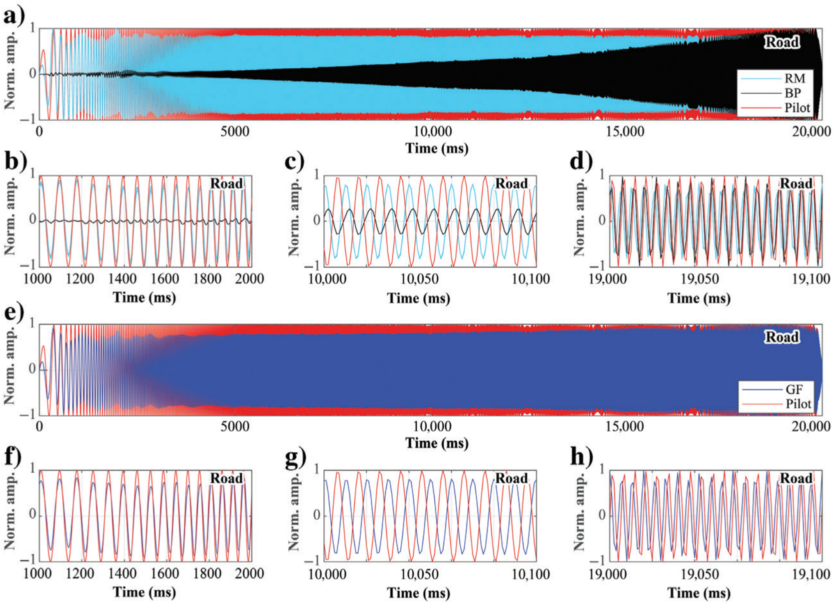

Figure 13. Evaluation of signals recorded with reaction mass (RM) and base plate (BP) accelerometers versus pilot signal (pilot) and computed ground force (GF) signal for the vibrating point located on asphalt. (a) Overlay of the BP, RM, and pilot signal for the entire 20 s sweep. (b-d) Enlarged views of the signals shown in (a) and times annotated on the lower axis of every plot. (e) Comparison of the pilot (red) versus the computed GF signal (blue) for the entire 20 s sweep. (f-h) Enlarged views of signals at the times annotated on the lower axis of every plot with colors corresponding to signals as annotated in legend in (e).

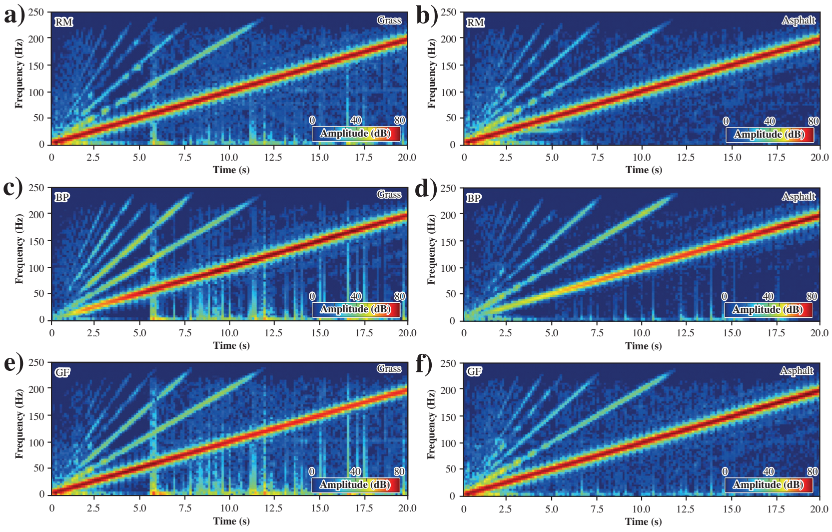

Figure 14. The FT-domain accelerometer signals and GF for vibrating points located on different surface conditions. The dynamic range of the FT spectrogram plots is 80 dB. RM, BP, and GF signals on the left side (a, c, and e) are with the source on grass, whereas the signals on the right side (b, d, and f) are with the source on asphalt.

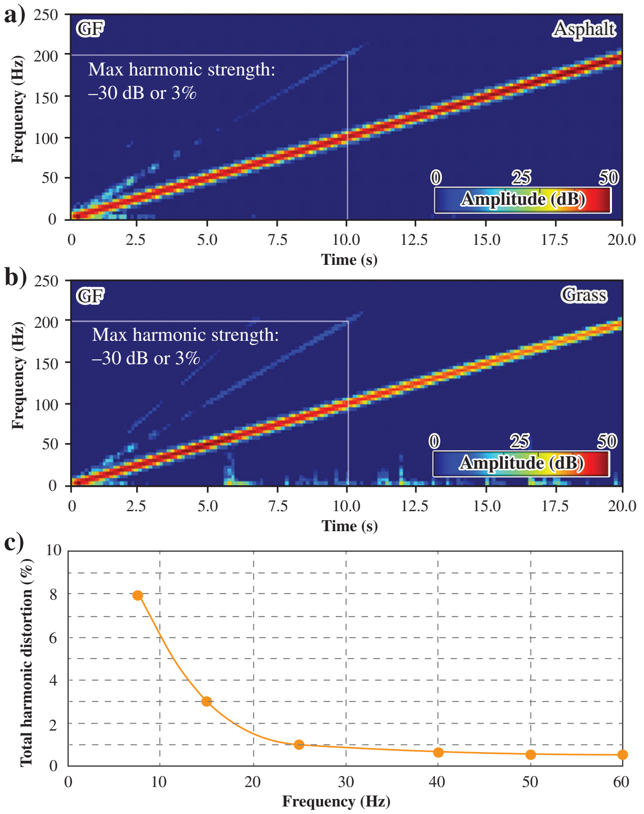

Figure 15. The GF spectrograms with dynamic range reduced to 50 dB for different ground conditions: (a) asphalt and (b) grass surfaces. Harmonic distortion is slightly higher on grass with the third harmonic visible. (c) THD (in %) averaged over grass and asphalt for the GF signal as a function of frequency. The dots represent the discrete frequencies in the FT domain used to calculate the THD as the amplitude ratio between the fundamental and the sum of the second, third, and fourth harmonic.

these claims, further analyses and a side-by-side comparison between the e-vib and a hydraulic vibrator at comparable force levels and same acquisition parameters are necessary.

CONCLUSION

The seismic imaging properties of an electric LSM-driven seismic vibrator (e-vib) were analyzed at a site in the central Netherlands. The source operated using a linear sweep of 1–200 Hz and drive level of 6.7 kN. Data were acquired along a 2D profile using a combination of geophone-nodal and MEMS-based landstreamer-mounted seismic recorders. Raw shot gathers of the nodal-landstreamer data set show strong reflections down to 1.25 s (1.3 km depth) and weakly visible events down to 1.5 s (1.8 km depth). The stacked section shows a good-quality high-resolution image with strong reflections seen from the top stratigraphic members shallower than 200 m down to 2 km deep ones, whereas reflections as deep as 2.9 km are visible. To obtain a reference for the imaging potential of the e-vib source, we have also processed a legacy 3D microspread acquired at the same site. Although the microspread was acquired using a significantly larger source (14.1 t, 67.6 kN), the 2D slices extracted from the processed NMO stack seismic volume show similar penetration depths and key reflections imaged on both data sets.

Harmonic distortion analysis shows that the e-vib harmonic distortion was slightly less on asphalt compared to grass, where, for both conditions, the harmonics are at least 30 dB down from the fundamental. In general, our results demonstrate that this small-scale vibrator with low harmonic distortion is capable of producing good-quality broadband seismic data, enabling high-resolution seismic imaging of the shallow and deep geologic settings. The results obtained are encouraging and show that the e-vib has good potential for high-resolution seismic imaging of different targets and depth ranges, such as for mineral and hydrocarbon exploration and geothermal applications.

ACKNOWLEDGMENTS

This pilot test study was carried out within the Smart Exploration project. Smart Exploration has received funding from the European Union's Horizon 2020 research and innovation program under grant agreement no. 775971. We thank R. Jenneskens for organizing the survey, along with S. Bakrac and M. Zhang from Delft Inversion, J. van den Berg from Delft University, W. Roefs from Seismic Mechatronics, and R. Plakane, M. Markovic, and G. Donoso from Uppsala University for their help during the data acquisition. Globe Claritas™ under license from the Institute of Geological and Nuclear Sciences Limited (GNS), Lower Hutt, New Zealand, was used to prepare and process the seismic data. Plotting was done using GMT from P. Wessel and W. H. F. Smith and MATLAB. We especially appreciate and thank G. Vermeer for providing the Shell microspread data used for comparison. We are grateful to C. Torres-Verdin, C. Krohn, T. Dean, and an anonymous reviewer for their helpful suggestions and comments that helped improve the quality of the paper.

DATA AND MATERIALS AVAILABILITY

Data associated with this research are available and can be obtained by contacting the corresponding author.

REFERENCES

Bagaini, C., 2008, Low-frequency vibroseis data with maximum displacement sweeps: The Leading Edge, **27**, 582–591, doi: 10.1190/1.2919575.

Bagaini, C., M. Laycock, C. Readman, E. Coste, and C. Anderson, 2014, Seismo-acoustic characterization of a seismic vibrator: 84th Annual International Meeting, SEG, Expanded Abstracts, 25–29, doi: 10.1190/segam2014-1126.1.

Brittan, J., and I. Jones, 2019, FWI evolution — From a monolith to a toolkit: The Leading Edge, **38**, 179–184, doi: 10.1190/tle38030179.1.

Brodic, B., A. Malehmir, C. Juhlin, L. Dynesius, M. Bastani, and H. Palm, 2015, Multicomponent broadband digital-based seismic landstreamer for near-surface applications: Journal of Applied Geophysics, **123**, 227–241, doi: 10.1016/j.jappgeo.2015.10.009.

Brodic, B., A. Malehmir, A. Pugin, and G. Maries, 2018, Three-component seismic land streamer study of an esker architecture through S- and surface-wave imaging: Geophysics, **83**, no. 6, B339–B353, doi: 10.1190/geo2017-0747.1.

Cordery, S., 2020, An effective data processing workflow for broadband single-sensor single-source land seismic data: The Leading Edge, **39**, 401–410, doi: 10.1190/tle39060401.1.

Dean, T., J. Quigley, S. MacDonald, and C. Readman, 2016, The design of optimized broadband vibroseis sweeps: The Leading Edge, **35**, 684–688, doi: 10.1190/tle35080684.1.

Dehghannejad, M., A. Malehmir, M. Svensson, M. Lindén, and H. Möller, 2017, High-resolution reflection seismic imaging for the planning of a double-train-track tunnel in the city of Varberg, southwest Sweden: Near Surface Geophysics, **1**, 1–15, doi: 10.3997/1873-0604.2017011.

Denis, M., V. Brem, F. Pradalie, F. Moinet, M. Retailleau, J. Langlois, B. Bai, R. Taylor, V. Chamberlain, and I. Frith, 2013, Can land broadband seismic be as good as marine broadband? The Leading Edge, **32**, 1382–1388, doi: 10.1190/tle32111382.1.

Drijkoningen, G. G., A. Veltman, W. Hendrix, K. Faber, J. Brouwer, and G. A. Hemstede, 2006, A linear motor as seismic horizontal vibrator: Near Surface Geosciences Conference and Exhibition, EAGE, cp-2-00315, doi: 10.3997/2214-4609.201402307.

Ghose, R., 2002, High-frequency shear wave reflections from shallow subsoil layers using a vibrator source: Sweep cross-correlation versus deconvolution with groundforce derivative: 72nd Annual International Meeting, SEG, Expanded Abstracts, 1408–1411, doi: 10.1190/1.1816924.

Kallweit, R. S., and L. C. Wood, 1982, The limits of resolution of zero-phase wavelets: Geophysics, **47**, 1035–1046, doi: 10.1190/1.1441367.

Kammann, J., A. Malehmir, B. Brodic, M. Tagliavento, L. Stemmerik, E. Nørmark, H. Lykke-Andersen, and L. Nielsen, 2019, Deep onshore reflection seismic imaging of the chalk group strata using a 45 kg accelerated weight-drop and combined recording systems with dense receiver spacing: Geophysics, **84**, no. 4, B259–B268, doi: 10.1190/geo2018-0755.1.

Kombrink, H., J. C. Doornenbal, E. J. T. Duin, M. den Dulk, J. H. ten Veen, and N. Witmans, 2012, New insights into the geological structure of the Netherlands; results of a detailed mapping project: Netherlands Journal of Geosciences — Geologie en Mijnbouw, **91**, 419–446, doi: 10.1017/S0016774600000329.

Levendal, T., D. Sopher, C. Juhlin, and O. Lehnert, 2019, Investigation of an Ordovician carbonate mound beneath Gotland, Sweden, using 3D seismic and well data: Journal of Applied Geophysics, **162**, 22–34, doi: 10.1016/j.jappgeo.2019.01.008.

Malehmir, A., G. Maries, E. Bäckström, M. Schön, and P. Marsden, 2017, Developing cost-effective seismic mineral exploration methods using a landstreamer and a drophammer: Scientific Reports, **7**, 1–7, doi: 10.1038/s41598-017-10451-6.

Malehmir, A., S. Wang, J. Lamminen, B. Brodic, M. Bastani, K. Vaittinen, C. Juhlin, and J. Place, 2015a, Delineating structures controlling sandstone-hosted base-metal deposits using high-resolution multicomponent seismic and radio-magnetotelluric methods: A case study from Northern Sweden: Geophysical Prospecting, **63**, 774–797, doi: 10.1111/1365-2478.12238.

Malehmir, A., F. Zhang, M. Dehghannejad, E. Lundberg, C. Döse, O. Friberg, B. Brodic, J. Place, M. Svensson, and H. Möller, 2015b, Planning of urban underground infrastructure using a broadband seismic landstreamer — Tomography results and uncertainty quantifications from a case study in southwestern Sweden: Geophysics, **80**, no. 6, B177–B192, doi: 10.1190/geo2015-0052.1.

Margrave, G. F., and M. P. Lamoureux, 2019, Numerical methods of exploration seismology: With algorithms in MATLAB®: Cambridge University Press.

Meunier, J., 2011, Seismic acquisition from yesterday to tomorrow: SEG, Distinguished Instructor Series.

Munsterman, D. K., R. M. C. H. Verreussel, H. F. Mijnlieff, N. Witmans, S. Kerstholt-Boegehold, and O. A. Abbink, 2012, Revision and update of the Callovian-Ryazanian stratigraphic nomenclature in the northern Dutch offshore, i.e. Central Graben Subgroup and Scruff Group: Netherlands Journal of Geosciences — Geologie en Mijnbouw, **91**, 555–590, doi: 10.1017/S001677460000038X.

Newman, B. J., 1994, The vibroseis exploration method, a processor's perspective: The Leading Edge, **13**, 664–668, doi: 10.1190/1.1437025.

Noorlandt, R., G. Drijkoningen, J. Dams, and R. Jenneskens, 2015, A seismic vertical vibrator driven by linear synchronous motors: Geophysics, **80**, no. 2, EN57–EN67, doi: 10.1190/geo2014-0295.1.

Ras, P., M. Daly, and G. Baeten, 1999, Harmonic distortion in slip sweep records: 69th Annual International Meeting, SEG, Expanded Abstracts, 609–612, doi: 10.1190/1.1821095.

Rijks Geologische Dienst, 1993, Geological atlas of the subsurface of The Netherlands: Explanation to Map V Sneek – Zwolle: Geological Survey of The Netherlands (RGD).

Rowse, S., and A. Tinkle, 2016, Vibroseis evolution: May the ground force be with you: First Break, **34**, 7, doi: 10.3997/1365-2397.34.1.83800.

Sallas, J. J., 1984, Seismic vibrator control and the downgoing P-wave: Geophysics, **49**, 732–740, doi: 10.1190/1.1441701.

Sallas, J. J., 2010, How do hydraulic vibrators work? A look inside the black box: Geophysical Prospecting, **58**, 3–18, doi: 10.1111/j.1365-2478.2009.00837.x.

Storm 7, seismic-mechatronics.com/seismic-sources/storm/, accessed 12 October 2020

Tellier, N., G. Ollivrin, and D. Boucard, 2014, Optimizing the generation and QC of low-dwell sweeps: Near Surface Geosciences Conference and Exhibition, EAGE, 1–5, doi: 10.3997/2214-4609.20140755.

ten Kroode, F., S. Bergler, C. Corsten, J. de Maag, F. Strijbos, and H. Tijhof, 2013, Broadband seismic data — The importance of low frequencies: Geophysics, **78**, no. 2, WA3–WA14, doi: 10.1190/geo2012-0294.1.

Teyssandier, B., and J. J. Sallas, 2019, The shape of things to come — Development and testing of a new marine vibrator source: The Leading Edge, **38**, 680–690, doi: 10.1190/tle38090680.1.

Vermeer, G. J. O., 2012, 3D seismic survey design, 2nd ed.: SEG, Geophysical References Series.

Wei, Z., 2009, How good is the weighted-sum estimate of the vibrator ground force?: The Leading Edge, **28**, 960–965, doi: 10.1190/1.3192844.

Wei, Z., and M. A. Hall, 2011, Analyses of vibrator and geophone behavior on hard and soft ground: The Leading Edge, **30**, 132–137, doi: 10.1190/1.3555320.

Wei, Z., and T. F. Phillips, 2013, On the generation of low frequencies with modern seismic vibrators: Geophysics, **78**, no. 2, WA91–WA97, doi: 10.1190/geo2012-0342.1.

Wei, Z., T. F. Phillips, and M. A. Hall, 2010, Fundamental discussions on seismic vibrators: Geophysics, **75**, no. 6, W13–W25, doi: 10.1190/1.3509162.

Wong, T. E., D. A. J. Batjes, and J. de Jager, 2007, Geology of the Netherlands: Edita-KNAW.

Biographies and photographs of the authors are not available.